Molecular Mechanism for Low pH Triggered Misfolding of the Human Prion Protein†

Mari L. DeMarco and Valerie Daggett*

Department of Medicinal Chemistry, Biomolecular Structure and Design Program, University of Washington, Seattle, Washington 98195-7610

Received September 13, 2006; Revised Manuscript Received January 16, 2007

ABSTRACT: Conformational changes in the prion protein cause transmissible spongiform encephalopathies, also referred to as prion diseases. In its native state, the prion protein is innocuous (PrP^C), but it can misfold into a neurotoxic and infectious isoform (PrP^{Sc}). The full-length cellular form of the prion protein consists of residues 23−230, with over half of the sequence belonging to the unstructured N-terminal domain and the remaining residues forming a small globular domain. During misfolding and aggregation, portions of both the structured and unstructured domains are incorporated into the aggregates. After limited proteolysis by proteinase K, the most abundant fragment from brain-derived prion fibrils is a 141-residue fragment composed of residues 90−230. Here we describe simulations of this fragment of the human prion protein at low pH, which triggers misfolding, and at neutral pH as a control. The simulations, in agreement with experiment, show that this biologically and pathologically relevant prion construct is stable and native-like at neutral pH. In contrast, at low pH the prion protein is destabilized via disruption of critical long-range salt bridges. In one of the low pH simulations this destabilization resulted in a conformational transition to a PrP^{Sc}-like isoform consistent with our previous simulations of a smaller construct.

Human (hu) PrP[1] expressed on the surface of cells is derived from a 253 amino acid polypeptide. On its way to the plasma membrane, both its N-terminal (residues 1−22) and C-terminal (residues 231−253) signal sequences are cleaved, glycans are covalently attached at Asn181 and Asn197, the disulfide bond is formed between helices B and C (HB and HC), and the glycosylphospatidylinositol (GPI) anchor is attached to the C-terminal serine. The resulting 208-residue diglycosylated protein is then targeted to lipid rafts on the membrane surface (Figure 1). Properly folded cell surface PrP (PrP^C) has a half-life of 3−6 h (*1*), and it can constitutively cycle between the cell surface and early endocytic pathway, each round trip taking approximately 60 min (*2*).

While PrP^C is innocuous, the protein can misfold into PrP^{Sc}, a species that has been identified as the causative agent in transmissible spongiform encephalopathies. PrP^C and PrP^{Sc} share the same covalent structure but possess different folds. Additionally, PrP^{Sc} is capable of aggregating into a variety of forms from amorphous to highly structured aggregates. In humans, PrP^{Sc} is responsible for Creutzfeldt−Jakob disease (CJD), fatal familial insomnia (FFI), Kuru, and Gerstmann−Sträussler−Scheinker disease (GSS), all of which are fatal neurodegenerative diseases. To prevent and treat these diseases, knowing where and how PrP^C converts to PrP^{Sc} is of interest. One plausible location for conversion that has been identified is the endocytic pathway (*3*, *4*).

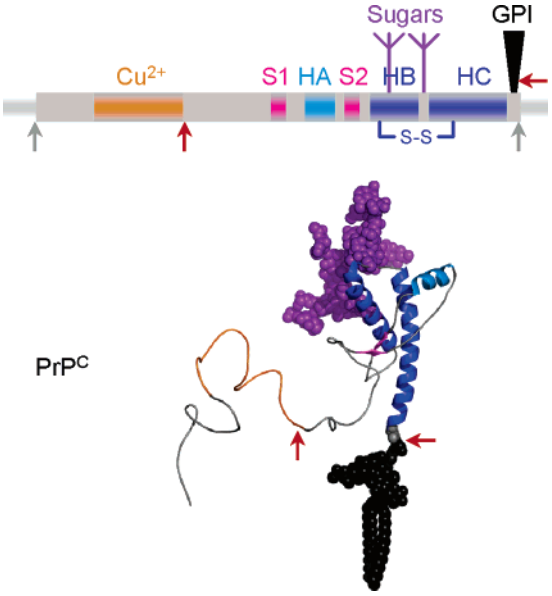

FIGURE 1: Sequence, structure, and clip sites of PrP. During the synthesis of PrP^C the N- and C-terminal signal sequences are cleaved (gray arrows). In the purification of PrP^{Sc}, the protein is enzymatically clipped at approximately residue 90 and at the GPI anchor (red arrows) forming PrP 27−30.

† We gratefully acknowledge partial support from the National Institutes of Health (Grant RO1 GM-50789 to V.D.) and a National Institute of General Medical Sciences National Research Service Award (Grant GM-07750) and the Hope Barnes Fellowship to M.L.D.

* Corresponding author. E-mail: daggett@u.washington.edu. Phone: (206) 685-7420. Fax: 206-685-3252.

[1] Abbreviations: PrP, prion protein; PrP^C, cellular prion protein; PrP^{Sc}, misfolded form of the prion protein; hu, human; SHa, Syrian hamster; MD, molecular dynamics; RMSD, root-mean-square deviation; RMSF, root-mean-square fluctuation; CJD, Creutzfeldt−Jakob disease; FFI, fatal familial insomnia

10.1021/bi0619066 CCC: $37.00
Published on Web 02/22/2007

Defining *where* conversion may occur has also led to plausible reasons as to *how* conversion is triggered. Endocytic organelles have a characteristically low pH (as low as pH 4.3 (*5*)), and this acidic environment triggers PrP misfolding *in vitro* (*6*). For a review of the numerous experiments linking PrP misfolding with a low pH environment readers are directed to ref *7*.

To study PrP^{Sc}, PrP^{C} converted (*in vivo* or *in vitro*) to PrP^{Sc} is purified by enzymatic and chemical treatments. The purification step results in increased order of the aggregate as well as partial proteolysis of N- and possibly C-terminal residues, where the aggregate (now a fibril) is termed PrP 27−30. PrP 27−30 (27−30 refers to the mass range in kDa of the PrP subunits and, although not explicitly stated, always refers to the PrP^{Sc} isoform) is the most abundant fragment in PrP fibrils and corresponds to residues ∼90−230 (Figure 1).

Based on the NMR structure of the $huPrP^{C}$ 90−230 fragment (1QLX (*8*)), the protein has a large unstructured domain (residues 90−124) and a globular domain (125−228) with three α-helices (HA, HB, and HC) and a short *β*-sheet (S1 and S2) (Figure 1). While the structure of PrP^{C} is known, there exists no experimental high-resolution structural information for PrP^{Sc} or for the pathway from PrP^{C} to PrP^{Sc}. PrP^{Sc} aggregates are heterogeneous both in structure and properties, thereby preventing the use of existing high-resolution structure determination methods. Molecular dynamics (MD) simulations represent another approach for mapping the conformational changes involved in the conversion of the prion protein. Our previous investigations of the misfolding pathway of wild-type (wt) hu, wt and mutated Syrian hamster (SHa), and mutated bovine PrP^{C} focused on the 109−219-residue fragment of the globular domain of PrP^{C} (*9*−*11*). For both the human and bovine forms the globular domain begins at residue 125. To generate equivalent constructs, residues 109−124 from a hamster structure (*12*) were grafted onto the human and bovine structures. It is important to include this N-terminal segment, as epitope mapping studies indicate that the C-terminal portion of PrP^{C} is largely unaltered as PrP^{C} converts to PrP^{Sc}, whereas the N-terminal portion undergoes extensive conformational rearrangement in which epitopes in the N-terminus are either altered or buried in PrP^{Sc} (*13*). Further support for large changes in the N-terminal region during conversion comes from protein engineering studies showing that this region is critical for PrP^{Sc} formation (*14*). In addition, a stop signal at residue 145 causes GSS and it eliminates essentially the entire structured C-terminal region (*15*), again highlighting the importance of the N-terminal region to the pathology. There is further discussion of this issue below and in a recent paper by DeMarco et al. (*7*).

Other research groups have also probed the structural and dynamic properties of PrP^{C} using MD simulations ranging in length from 1 to 10 ns, with most about 1 ns in length (*16*−*24*). These other studies used smaller constructs omitting the unstructured, N-terminal region, typically beginning at residue 125. In addition, several of these simulations have the disulfide bond reduced, although experiments indicate that it remains oxidized *in vivo* and that an intact disulfide bond is necessary for infectivity (*25*−*28*). So, these studies can address the conformational behavior of the structured domain and assume that it reflects the behavior of the larger constructs, but the N-terminus should be present to investigate effects relevant to the pathology.

Consequently, to build upon the previous studies and to match the more commonly used experimental construct (residues 90−230), we modeled the unstructured residues, 90−124 and 229−230, onto the NMR structure of $huPrP^{C}$. This construct encompassed our previously studied construct (residues 109−219), as well as the only known neurotoxic peptide (106−126) (*29*, *30*), and the toxic and infectious $PrP^{Sc}106$ (also known as mini-PrP, residues 90−230, Δ141−176) (*31*). Here we describe MD simulations of $huPrP^{C}$ (residues 90−230) at both neutral and low pH to determine the effect of lowering the pH on PrP structure and dynamics.

METHODS

The starting structure for the simulations was the $huPrP^{C}$ NMR structure (1QLX (*8*)). Since the NMR structure contains only residues 125−228, residues 90−124 and residues 229−230 were modeled onto the globular domain to yield the 90−230 construct. The N-terminal region was modeled in two steps. First residues 109−124 were modeled in based on the NMR structure of $SHaPrP^{C}$, which begins at residue 109 (structure provided by T. L. James and S. Farr-Jones (*12*)). Second, an unstructured sequence, residues 90−108, was then modeled onto the 109−228 construct. Since modeling residues 90−108 could potentially bias the results of the simulations, we attempted to minimize such bias by adding a segment with no repeating secondary structure and no interactions between residues within the segment and between the modeled segment and the globular region. The secondary structure of the residues within the modeled segment (residues 90−108), as calculated using the DSSP algorithm (*32*), are (beginning at residue 91) UUU*β*UUUHUUHUU*ββ*U*ββ* where H = helix, *β* = *β*-structure, and U indicates that the individual residue is neither helical, *β*, nor extended. Finally, the missing two C-terminal residues were added. The disulfide bond was left intact for all simulations.

MD simulations were performed using our in-house program *in lucem* molecular mechanics (*il*mm) (*33*), which employs the Levitt *et al.* force field (*34*, *35*) and the microcanonical (NVE) ensemble (*36*). All protein and water atoms were explicitly represented. To model the low pH environment of endosomes (pH 4.3−6) (*5*) and *in vitro* conversion of human PrP (*6*), we protonated Asp (pK_a ∼ 4.5), Glu (pK_a ∼ 4.6) and His (pK_a ∼ 6.2) residues. The next relevant pK_a is that of the terminal carbonylate, which is protonated at ∼pH 3.1, therefore by protonating Asp, Glu, and His we achieved a pH range of approximately 3.2−4.7, which falls within the pH range of both endosomal pH and *in vitro* conversion conditions. Neutral pH simulations correspond to a pH of ∼7, falling between the pK_as of His side chains and the main chain α-amino group (6.8−7.9). The pK_a values given are only approximations as they are highly dependent on the local environment. A recent theoretical investigation of His pK_as in PrP^{C} demonstrates the range of possible values (*37*).

After setting the ionization states, the protein was minimized for 1000 steps *in vacuo* and then solvated in a rectangular box with water extending at least 10 Å from any protein atom. All simulations were run at 298 K with the

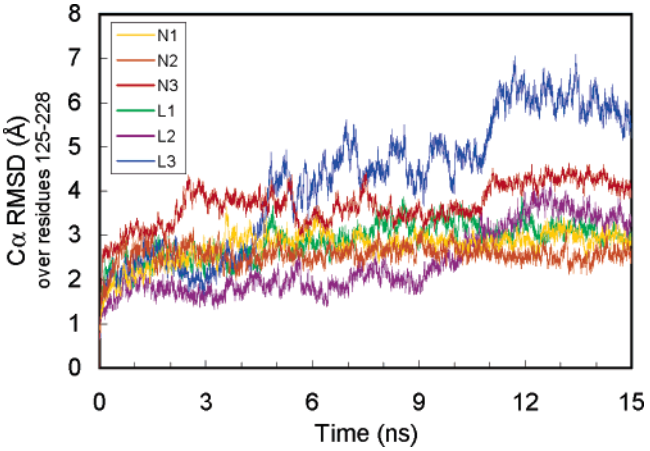

FIGURE 2: Cα RMSD of the structured region of huPrP^C, residues 125−228.

water density set to the experimental value of 0.997 g/mL (*38*), by adjusting the box volume. The systems were further equilibrated for 1000 steps of minimization, 2500 steps of MD of water, 500 steps of minimization, 2500 steps of MD of PrP, and a final 500 steps of minimization. A 10 Å force-shifted nonbonded cutoff was used (*36*). The nonbonded list was updated every 5 steps. A time step of 2 fs was used. Each simulation was carried out for 15 ns, with structures saved every 0.2 ps for analysis.

Secondary structure analysis was based on (ϕ,ψ) angles where only repeating structure (three or more residues in the same conformation) was considered. Hydrogen bond networks were identified by geometrically defined criteria (*39*) and displayed using UCSF Chimera software (*40*). All molecular graphics images were produced using UCSF Chimera (*40*).

RESULTS

Six simulations using huPrP^C 90−230 as a starting structure were performed: three at neutral pH (N1, N2, and N3) and three at low pH (L1, L2, and L3). With the relatively long disordered N-terminus, all simulations were monitored for potential periodic contacts. All simulations maintained zero contacts with their periodic images except L1. In L1, one residue pair transiently interacted through the periodic box for a total of 18 ps of the 15 000 ps trajectory, or 0.12% of the time (at 3.411−3.427, 3.437, and 3.788 ns). To quantitatively assess structural similarity/dissimilarity over time as compared to the starting PrP^C structure, Cα root-mean-square deviations (RMSDs) were calculated for the globular region (residues 125−228, Figure 2), and the average values over the last 10 ns of simulation time can be found in Table 1.

Cα root-mean-square fluctuations (RMSFs) were calculated for each simulation to monitor the degree of motion of individual residues relative to the average structure populated (Figure 3A). To visually demonstrate the dynamics of the main chain, snapshots taken at 3 ns granularity from selected simulations are shown in Figure 3B. By superimposing structures and aligning them by Cα atoms from HB and HC (which are linked by the disulfide bond) the dynamics of the N-terminal region is evident. A representative neutral pH simulation is displayed (N1) as well as two low pH

Table 1: Summary of Cα RMSD and Cα RMSF Results for the Last 10 ns of the MD Simulations

	globular domain[a] (last 10 ns)		entire protein		unstructured N-terminus[b]		globular domain	
	Cα RMSD (Å)	std dev	Cα RMSF (Å)	std dev	Cα RMSF (Å)	std dev	Cα RMSF (Å)	std dev
N1	2.8	0.3	1.8	0.3	2.1	0.4	1.7	0.3
N2	2.6	0.2	1.9	0.4	2.3	0.4	1.8	0.3
N3	3.7	0.4	1.9	0.4	2.3	0.5	1.8	0.3
L1	2.9	0.4	2.0	0.5	2.5	0.5	1.9	0.3
L2	2.4	0.7	2.0	0.5	2.3	0.4	1.9	0.4
L3	4.3	1.4	1.9	0.4	2.1	0.4	1.8	0.3

[a] Residues 125−228. [b] Residues 90−124.

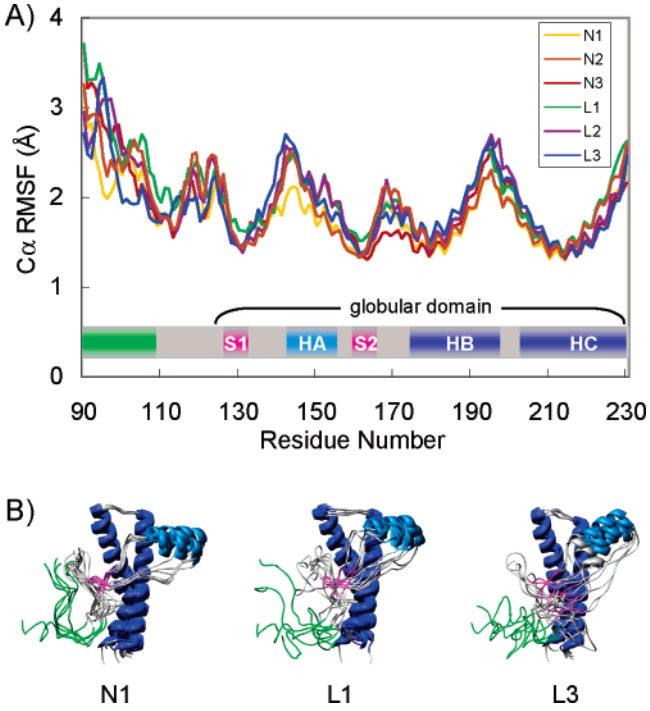

FIGURE 3: (A) Cα RMSF of huPrP for neutral and low pH simulations and (B) the dynamics of representative PrP simulations. Note that rotational motion is not removed from the RMSF calculations.

simulations, one with high Cα RMSFs and RMSDs (L3) and one with high Cα RMSFs and low (neutral pH-like) Cα RMSDs (L1). The values for all simulations are provided in Table 1.

To identify simulations where misfolding to PrP^{Sc}-like structures occurred, we evaluated main chain−main chain hydrogen bonds participating in extended sheets. Only one simulation, L3, had a significant increase in strand-to-strand hydrogen bond networks (extended sheets). Snapshots from L3 are provided in Figure 4, along with N1 as a control. The results for N1 are typical of all the neutral pH simulations. Unlike L3, in L1 and L2 the hydrogen bond network remained similar to the starting structure and conversion did not occur.

Upon inspection of structures from L3, the increase in hydrogen bonding was due to the formation of two new extended sheets. By 6 ns, the number of main chain−main chain hydrogen bonds involved in sheet formation in L3

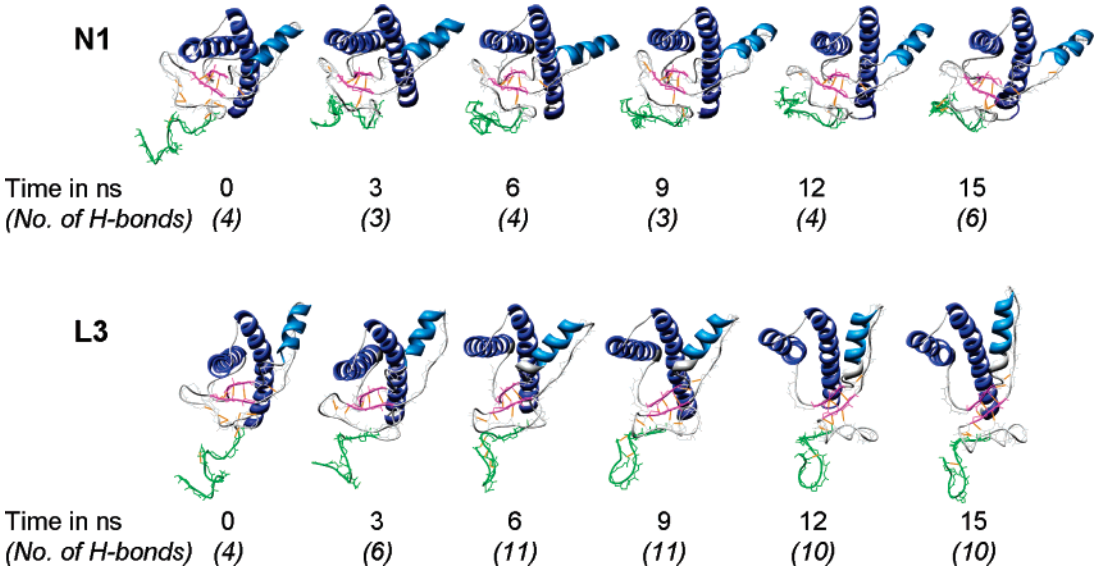

FIGURE 4: Comparing snapshots from a native state and a conversion trajectory. Structures from a neutral (N1) and low pH (L3) trajectory are colored based on the NMR defined secondary structure, with N-terminal residues 90−108 colored green. Main chain−main chain hydrogen bonds (orange lines) are represented (excluding those found within the native helices). The number of main chain−main chain hydrogen bonds that are involved in a sheet or result in sheet formation is given in parentheses.

increased from four (in the PrP^C starting structure) to 11 (Figure 5). In the starting structure three hydrogen bonds are found between S1−S2 and one above the S1−S2 sheet (toward the C-terminus of HA). The initial S1−S2 sheet acted as a template onto which an additional strand added. The resulting hydrogen bond network was composed of three strands: 119−121, 126−131, and 161−163 (Figure 5). In addition, a hairpin, independent of the three-stranded sheet, formed at the very N-terminus over residues 90−102. The hydrogen-bonding network fluctuated, but overall, it was maintained throughout the remainder of the simulation.

Using a combination of hydrogen bond networks and repeating (ϕ,ψ) secondary structure analysis, the amount of mixed α/β-sheets in the L3 misfolded ensemble (6−15 ns) was determined. There were 36 residues in repeating extended conformation: 90−95, 98−102, 119−121, 126−134, 137−139, 160−165, and 196−199. New strands are denoted: E1 (90−95), E2 (98−102), E3 (119−121), E4 (126−134), E5 (137−139), and E6 (160−165). In L3, extended structure rose from 4% in the starting structure to 26% in the misfolded ensemble. The 8 ns snapshot from the misfolded ensemble is shown in Figure 6.

In L3, the conformational conversion creates a large hydrophobic region on the solvent exposed surface of the protein (red residues in Figure 6). Unlike the scattered positioning of surface hydrophobic residues in PrP^C, as L3 forms the E3−E4−E6 sheet, hydrophobic residues coalesce to form a large solvent-exposed hydrophobic cluster. This motion is correlated with a modest overall increase in nonpolar solvent accessible surface area from 5313 $Å^3$ in the starting structure to an average of 5460 $Å^3$ in the misfolded ensemble.

At both neutral and low pH, HA, HB, and HC remained folded. In neutral pH simulations, the position of HA was relatively fixed, whereas in the low pH simulations, the position of HA fluctuated considerably with respect to the disulfide linked HB−HC platform (Figure 7). In the NMR structures, and in neutral pH simulations, HA is tethered to the HB−HC platform through hydrophobic contacts (primarily between S2 and HB), salt bridges, and side chain packing between HA and HC. In the low pH $huPrP^C$ simulations, HA becomes "disconnected" from the HB−HC platform. Note, we use "disconnected" to describe the sliding of HA about the HB−HC platform—it is not meant to imply complete dissociation and solvation of HA.

The disconnection of HA can be attributed to the low pH environment, which results in the abolition of two key long-range salt bridges. (The term long-range is used with respect to sequence separation to describe an interaction between residues separated by more than 4 residues, whereas a short-range interaction describes those between residues separated by 4 or fewer residues.) In general, short-range interactions are generally involved in stabilizing secondary structure whereas long-range interactions are important for maintaining tertiary structure. In the starting structure two long-range salt bridges pin the N-terminal portion of the structured domain (S1−HA−S2−loop) to the HB−HC scaffold: Arg156−Glu196 and Arg164−Asp178 (Figure 8). A short-range interaction extends the last salt bridge making the following network: Asp167−Arg164−Asp178. These two long-range salt bridges are well-maintained in all neutral pH simulations (Table 2). Additionally, a new long-range salt bridge formed in N1 and N3 between Glu146 and Arg208 (Figure 8), reinforcing the connection between the N- and C-terminal portions of the structured domain (Table 2). In all three neutral pH simulations, the short-range salt bridge Arg164−Asp167 broke at times without affecting the Arg164−Asp178 salt bridge.

In the three low pH simulations, neutralizing Asp and Glu disrupts both long-range salt bridges/networks present in the starting structure (Arg156−Glu196 and Arg164−Asp178) and also prevents the formation of the Glu146−Arg208 salt bridge (Table 2). In L2, the Asp167−Arg164−Asp178 network is disrupted but by the end of the simulation, Arg164 and Asp178 repacks to form a hydrogen bond between the

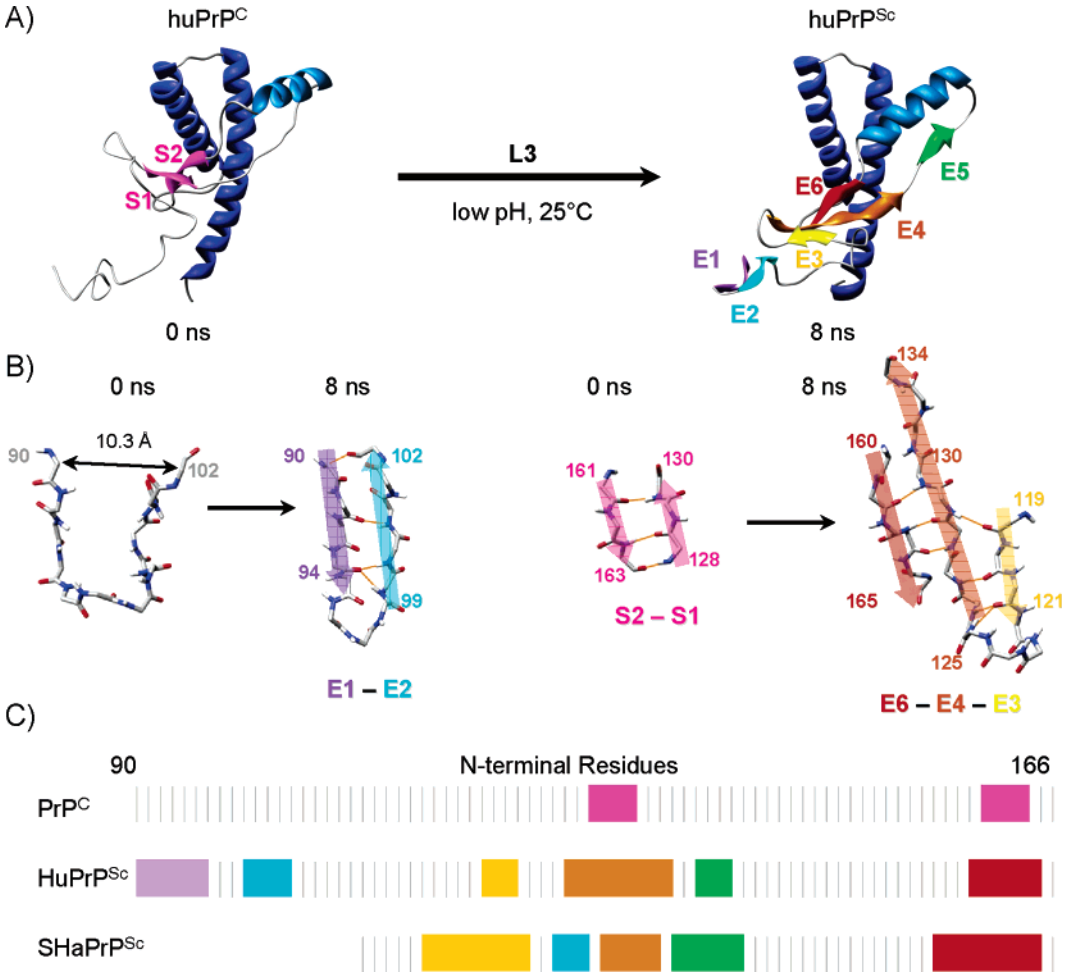

FIGURE 5: The hallmark of $PrP^C \rightarrow PrP^{Sc}$ transition: extended-structure formation. (A) Snapshots from L3 of the starting structure and the 8 ns structure from the misfolded ensemble. (B) Consistent with experiment, the N-terminal domain underwent a significant conformational transition (portions of the main chain shown, colored by atom type). (C) Comparison of the extended structure in the N-terminus of the NMR structure of $huPrP^C$, the misfolded ensemble from L3 ($huPrP^{Sc}$), and the misfolded ensemble from a previous conversion simulation of a mutated Syrian hamster PrP ($SHaPrP^{Sc}$ D147N). N-terminal residues that are in repeating extended conformation are denoted (colors correspond to the ribbon representation in A). A fragment of the protein, residues 90−166, is shown for the human constructs, and residues 109−166 are shown for the SHa since the simulation was of a smaller construct spanning residues 109−219.

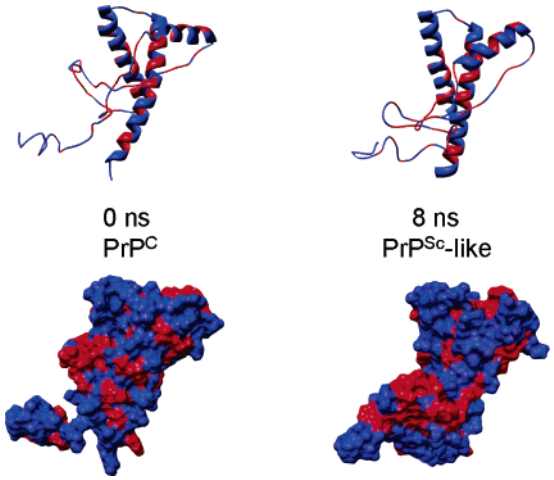

FIGURE 6: Formation of solvent exposed hydrophobic cluster in $PrP^C \rightarrow PrP^{Sc}$. Snapshots in space-filling mode from the L3 simulations are colored by polar (blue) and nonpolar (red) residues (hydrogens removed).

two side chains. In L1 and L3, the disruption of the long-range salt bridges partially releases HA and the nearby S1−S2 sheet from the HB−HC platform.

DISCUSSION

Based on experiment we expected that PrP^C would remain stable at neutral pH, while at low pH it would be destabilized and misfold. Based on the Cα RMSD of the globular region (residues 125−228), the structured region remains relatively native-like for all simulations, with some exceptions in L3. This does not, however, mean that they all behave like native-state simulations. The three neutral pH simulations have lower Cα RMSFs over the globular region as compared to the low pH simulations. This reflects the kinetic instability induced by protonation of the Asp, Glu, and His residues, as has been observed in previous neutral versus low pH simulations of PrP (*9*−*11*). Consequently, low pH, in agreement with experiment and previous MD simulations, destabilizes $huPrP^C$.

HA is rich in charged residues, and when some of these residues are protonated at low pH we might expect to observe two effects: partial unfolding of HA and "disconnection" of HA from the HB−HC scaffold. The importance of charge−charge interactions in stabilizing HA has been put forth in a theoretical prediction (*41*) that is commonly incorrectly cited as evidence for HA unfolding during conversion. Experiments have demonstrated that the disrup-

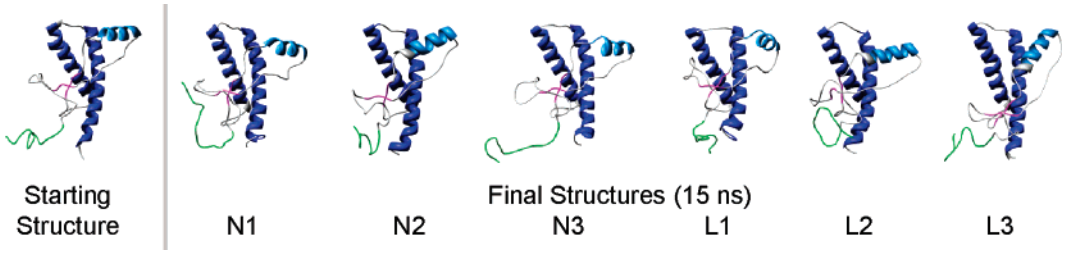

FIGURE 7: Snapshots of the final structures in each of the simulations (ribbon diagrams with helices shown, colored based on the minimized structure).

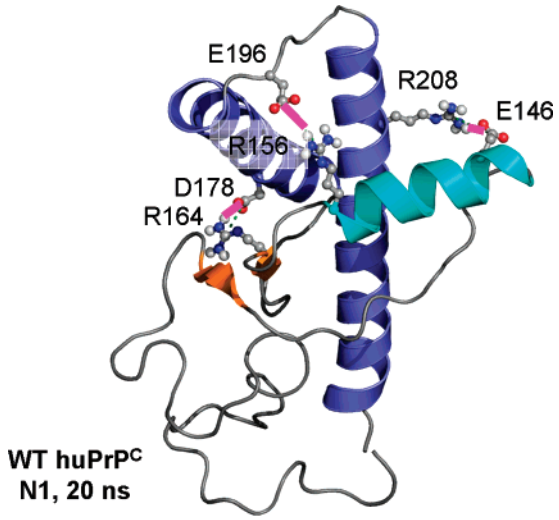

FIGURE 8: Salt bridges involved in tethering HA to the structured C-terminal portion of the protein. The Glu146−Arg208 is nonnative and is acquired during MD at neutral pH. The salt bridges are highlighted by magenta bars.

Table 2: Formation and Disruption of Long-Range Salt Bridges

	Arg156−*Glu196*[a]	Arg164−*Asp178*[c]	*Glu146*−Arg208[c]
in NMR structure?	yes	yes	no
neutral pH simulations[b]	N1, N2, N3	N1, N2, N3	N1, N3
low pH simulations[b]			

[a] Residues protonated (neutralized) at low pH are italicized. [b] For all simulations a salt bridge is considered intact if it is maintained, or in the case of Glu146−Arg208, is formed over the final 5 ns of simulation [c] Known disease-related genetic mutations that should disrupt the salt bridges: Asp178Asn, Arg208His, and Glu196Lys.

tion of salt bridges within HA does not disrupt HA (*42*), and, in fact, the HA sequence is nonamyloidogenic and generally slows conversion rates when present (*43*). High-temperature simulations of PrP^C have shown HA to be resilient (ref *44* and unpublished data), and this observation is mirrored in experiments of PrP-derived peptides in which HA under various conditions (low pH, high salt, organic cosolvents) remains helical (*45*). Furthermore Watzlawik and co-workers (*46*) have shown that HA (residues 144−154) is not converted to β-structure by comparing PrP fragments 23−144 and 23−159, which correspond to the human disease related 145 and 160 stop mutants. Interestingly, the longer fragment aggregates more rapidly, which given the lack of conversion of HA is probably due to the added stability of the residues C-terminal to HA compensating for the lack of S2.

We have previously demonstrated that the complete unfolding of HA is not necessary to produce misfolded species in agreement with experimental observables for PrP^{Sc} (*7*, *9*−*11*). With most of HA, HB, and HC intact, PrP can accommodate enough extended structure to account for the 43−54% extended structure observed in CD and IR spectra of PrP 27−30 fibrils (residues ∼90−230) (*47*−*49*). While we do not observe unfolding of HA in the $huPrP^C$ low pH simulations, we do observe the "disconnection" of HA from the HB−HC platform. In previous simulations of $SHaPrP^C$ at low pH specifically addressing mutations that knocked out salt bridges in HA, this same disconnection was observed with HA sliding both clockwise and counterclockwise about the HB−HC platform (*11*).

We have now been able to pinpoint a cause of HA sliding: the disruption of long-range salt bridges. In particular, the disruption of two long-range salt bridges results in the displacement of HA as well as the S1−S2 sheet (Table 3). One of these salt bridges forms a network linking the loop between S2 and HB to the HB−HC platform. A recently engineered PrP^C mutant with an additional disulfide between Cys166 and Cys221 (*50*) essentially serves the same function, linking the loop to the HB−HC platform. The relevance of this mutant is that it increases the structural stability of PrP^C and reduces its ability to misfold into a β-sheet rich structure (*50*). From simulation, the detachment of the N-terminal portion of the globular domain (S1−HA−S2) from the rigid C-terminal portion (HB−HC) accommodates misfolding. If on the other hand the salt bridges are intact or an even stronger anchor such as a covalent bond is substituted for the salt bridges (*50*), misfolding of PrP^C is less favorable. While low pH is known to destabilize and initiate misfolding of PrP^C, the current simulations in combination with experimental results provide a mechanism for this destabilization. We find that the low pH environment disrupts salt bridges neighboring the S1−S2 sheet, significantly alters its location and solvent accessibility. The unfavorable solvation of the sheet aids in the addition of a new strand (E3) (Figure 5), and the disconnection of the N- and C-terminal portions of the globular domain facilitates the formation of nonnative structure.

In the case of hereditary forms of FFI and CJD, a mutation at position 178 (Asp178 → Asn) is linked to disease (*51*). This mutation, like the protonation of Asp178 in a low pH environment, knocks out the native Arg164−Asp178 long-range salt bridge. In the absence of the salt bridge, $huPrP^C$ misfolding is facilitated. MD simulations of the globular fragment of $huPrP^C$ (*19*, *22*) and mouse PrP^C (*21*) at neutral pH with the Asp178Asn mutation have demonstrated that the abolition of the Arg164−Asp178 salt bridge is not particularly destabilizing. Our results suggest that disruption of Arg164−Asp178, along with the disruption of other key

Table 3: Disruption of Key Salt Bridges at Low pH Facilitates Conversion of PrP

key salt bridges			effect of low pH	
		role of salt bridges in PrPc	initial action	consequence
Arg 156	*Glu196*	anchors HA to the HB−HC platform	HA not anchored to HB−HC platform	HA slides along surface of HB−HC, only bound by hydrophobic contacts
Asp 167	Arg164	form network linking S2 and	S2 and S2−HB loop region not	S1−S2 sheet moves away from HB,
Asp178	Arg164	the S2-HB loop to HB	anchored to HB	disrupting core packing

tertiary contacts at low pH, can trigger changes in the N-terminal region.

Another known genetic mutation associated with CJD is Arg208His (*51*). In two of the neutral pH simulations, Arg208 (in HC) makes a stable salt bridge with Glu146 (in HA) (Table 2). Upon protonation of Glu146, this stabilizing long-range salt bridge does not form. The substitution of the shorter His side chain at residue 208 may not be able to make the same interactions/salt bridge as the longer Arg. Finally, substitution of Glu 196 for Lys leads to CJD (*51*). Thus, there are human disease-causing mutations affecting all three of the salt bridges identified by MD to be important in discouraging conversion, including one not present in the NMR structure. Specifically, D178N, E196K, and R208H, which should obliterate their respective salt bridges, are all fatal in humans (*51*).

All simulations had high fluctuations in the unstructured N-terminus, as expected (Table 1), but L3 had slightly lower fluctuations over residues 100−124 compared with the other low pH simulations (Figure 3A and Table 1). It is in this region that L3 formed novel extended structure, as was also observed in our earlier simulations. The formation and docking of these new strands account for the decreased fluctuations. In particular, in L3, residues 119−121 hydrogen bond to S1, locking them in place. The sequence N-terminal to residue 119 packs against HC and the sheet, contributing to the observed increased kinetic stability. Unlike L3, L1 and L2 do not form new stabilizing structure. In general, losing the salt bridges exacerbates the instability of the N-terminal region, as it disrupts the core and sets part of the globular region (residues 125−170) in motion, the consequences of which filter down to the N-terminus. This was the case for all low pH simulations, but in L3 the region stabilized after formation of new sheets.

The increase in extended structure at the N-terminus is consistent with a wealth of data implicating this region in conversion. In particular, residues 90−120 are antigenically accessible in PrP^C and encrypted in PrP^{Sc} (*52*). In contrast, HC is accessible to antibody in both forms. More recently Matsunaga et al. (*53*) expanded upon this work and used antibodies to probe the structure of rec-ShaPrP (residues 90−231) over a pH range of 2−12. The results of this anti-PrP antibody binding study indicate that the conformations of epitopes localized in the C-terminus are insensitive to pH, whereas the conformations of N-terminal residues are pH sensitive. Below pH 4, there is a significant decrease in binding of antibodies that target N-terminal epitopes.

Work by Swietnicki et al. (*6*) on an acid-induced unfolding intermediate of huPrP suggests that the bulk of the change in the structure upon conversion occurs over residues 90−127. A mini-prion containing residues 89−140 and 177−231 is infectious, suggesting that one of these two regions is critical to the conformation change but that residues 141−176 are dispensable (notably containing HA and S2) (*31*, *54*−*55*). Moreover, a peptide containing residues 90−144 with the P101L mutation fold into a β-rich structure that can cause prion disease in transgenic mice (*56*). There are also stop mutants at residues 145 and 160 in humans that cause disease (*51*); these mutations remove all three of the helices, and HB and HC, respectively. Consequently, conversion of these helices is not necessary for disease, while the N-terminus is. Lührs et al. (*57*) just reported a study of amyloid formation of various PrP constructs (different lengths and different sequences) in phospholipid bicelle solutions to better mimic the lipid raft environment the protein experiences *in vivo*: they concluded that residues 105−120 must be present for formation of PrP^{Sc}. Furthermore, residues 106−126 are neurotoxic (*30*, *58*). Because PrP(121−231) is not scrapie competent and not neurotoxic, residues 90−120 must be of paramount importance. This is where we see the bulk of our conversion here and in previous studies, and the experimental findings stress the importance of including the N-terminal segment in simulations.

During the misfolding process of $huPrP^C$, extended structure increased from 4 to 26%. The only available experimental constraint for the amount of extended structure in misfolded PrP species is of PrP 27−30 fibrils, with 43−54% extended structure (*47*, *49*). While the extended structure in the misfolded ensemble of L3 lies outside the experimental range, it is consistent with the trend of increased extended structure formation. We must also keep in mind that the experimental range comes from mature aggregates that have been chemically and enzymatically treated to consolidate structure while we are attempting to model the prefibrillar species. Nevertheless, the position of extended structure within our model is consistent with solid-state NMR studies of a PrP-derived peptide (*59*). In addition, the positions of the new strands E1 (90−94) and E2 (99−102) is interesting since proteinase K digestion results in preferred cleavage sites at 89, corresponding to type 1 prion strains, or at 98 for type 2 (*60*). There is also general agreement between the sites of conversion described here and in our earlier ShaPrP simulations (Figure 5).

ANS binding experiments suggest that there is an increase in nonpolar solvent accessible surface area upon conversion (*6*). We do not observe a significant trend in higher total nonpolar solvent accessible surface area in the low pH simulations. However, in the conversion trajectory (L3) N-terminal hydrophobic residues coalesce to form a continuous hydrophobic surface, consistent with an ANS binding site (Figure 6). The formation of the E3−E4−E6 sheet (Figure 5) presents this large, continuous hydrophobic patch, which has also been identified as a probable aggregation site (*11*, *61*).

The other proposed complementary oligomerization site, E5, began as an MD prediction (*11*), and it has since been

supported by a variety of experimental observations. The observed E5 strand is in agreement with NMR studies of PrP peptides from this region, which have a tendency to form extended structure (*45*). This strand is found in an isolated hydrophobic stretch (residues 137−142: Pro-Ile−Ile-His-Phe-Gly). Recently Ziegler et al. (*43*) found that this region has a high aggregation propensity via turbidimetric aggregation assays. Further support for this region forming extended structure and being involved in PrP^{Sc} aggregation comes from peptide inhibitors derived from the PrP sequence (*61*). PrP peptides spanning this region aggregate to form fibrils and can also act to inhibit PrP aggregation (*61*). Kundu et al. (*62*) also found that the critical amyloidogenic region extends beyond the N-terminus to our E5 segment and this region is essential for nucleating oligomerization. Thus, CD, NMR, peptide aggregation, peptide inhibitor, and PrP aggregation studies give us reason to suspect that the region between S1 and HA is important in PrP^{Sc} oligomer formation, and our MD studies provide atomic resolution models that account for these findings.

In addition to extended structure formation, the amount and location of α-helix can help determine the presence of a PrP^{Sc}-like species. In highly ordered PrP^{Sc} fibrils, PrP subunits contain α-helix in the range of 21−30% (*47*−*49*), a drop from 35% in the NMR structure if corrected for the difference in size of the constructs (*8*). Antibody mapping studies have revealed that the helical structure in PrP^{Sc} is native (PrP^{C}) helix. Consistent with experiment, in both the neutral and low pH $HuPrP^{C}$ simulations, the native helices are largely maintained. The mapping studies also identified specific regions of HA, HB, and HC that are maintained (both in structure and accessibility) during conversion. Several nonselective antibodies, antibodies that bind both PrP^{C} and PrP^{Sc}, have been mapped to HA (*52*, *63*−*65*), the N-terminus of HB (*65*), and the C-terminus of HC (*66*). All trajectories preserve these epitopes. Furthermore, the 6H4 antibody, which recognizes an epitope in HA, precipitates both PrP^{C} and PrP^{Sc} (*67*), indicating that HA remains intact through the conversion process. A detailed comparison of PrP^{C} and PrP^{Sc} structure and PrP selective and nonselective antibodies has been presented previously (*7*, *11*). Based on the early misfolded species identified in L3, the antibody mapping studies, and FTIR and CD spectroscopy of PrP^{C} and PrP^{Sc} fibrils, we might expect some minor, localized unfolding of the native helices (likely between the C-terminus of HB and the N-terminus of HC and possibly the C-terminus of HA) as conversion progresses, as has been observed in our previous simulations.

CONCLUSIONS

The misfolding of $huPrP^{C}$ involves a partial unfolding and misfolding step. In one of our low pH simulations we observe these steps as PrP^{C} converts to a PrP^{Sc}-like structure rich in extended structure. Misfolding is a rare event, and we do not expect to see it in every simulation. As is the case with many of our low pH simulations, two of the three simulations presented here did not convert into a PrP^{Sc}-like isoform. However in all cases, we observed the partial unfolding and disconnection of helix HA. This disconnection of HA can be attributed to the low pH environment, which results in the abolition of two key long-range salt bridges. In the starting structure these salt bridges pin the N-terminal portion of the structured domain (S1−HA−S2−loop) to the C-terminal portion (HB−HC): R156−E196 and R164−D178. These salt bridges are maintained in all three neutral pH simulations. Additionally, a new, nonnative, long-range salt bridge forms during MD at neutral pH between E146 and R208, reinforcing the connection between the N- and C-terminal portions of the structured domain. Neutralizing Asp and Glu at low pH disrupts both long-range native salt bridges, as well as preventing formation of the nonnative salt bridge. The disruption of these long-range salt bridges removes the structural tethers keeping HA close to the HB−HC scaffold, and consequently HA and the nearby S1−S2 sheet become dislodged. All three of these salt bridges are associated with known disease-causing genetic mutations: R208H, D178N, and E196K. Loss of these salt bridges by mutation is expected to be similar to removing them through protonation, such that conversion drastically changes the surface properties of PrP on one face of the molecule, presenting large hydrophobic segments prone to aggregation, while on the other face (HB−HC region), PrP remains native-like. The results from this MD study of huPrP (90−228) provide atomic-resolution views of the initial conversion PrP may undergo in human neurodegenerative diseases such as CJD, FFI, Kuru, and GSS.

REFERENCES

1. Caughey, B., Race, R. E., Ernst, D., Buchmeier, M. J., and Chesebro, B. (1989) Prion Protein-Biosynthesis in Scrapie-Infected and Uninfected Neuro-Blastoma Cells, *J. Virol. 63*, 175−181.
2. Harris, D. A., Huber, M. T., Vandijken, P., Shyng, S. L., Chait, B. T., and Wang, R. (1993) Processing of a Cellular Prion Protein - Identification of N-Terminal and C-Terminal Cleavage Sites, *Biochemistry 32*, 1009−1016.
3. Arnold, J. E., Tipler, C., Laszlo, L., Hope, J., Landon, M., and Mayer, R. J. (1995) The Abnormal Isoform of the Prion Protein Accumulates in Late-Endosome-Like Organelles in Scrapie-Infected Mouse-Brain, *J. Pathol. 176*, 403−411.
4. Borchelt, D. R., Taraboulos, A., and Prusiner, S. B. (1992) Evidence for Synthesis of Scrapie Prion Proteins in the Endocytic Pathway, *J. Biol. Chem. 267*, 16188−16199.
5. Lee, R. J., Wang, S., and Low, P. S. (1996) Measurement of endosome pH following folate receptor-mediated endocytosis, *Biochim. Biophys. Acta 1312*, 237−42.
6. Swietnicki, W., Petersen, R., Gambetti, P., and Surewicz, W. K. (1997) pH-dependent stability and conformation of the recombinant human prion protein PrP(90−231), *J. Biol. Chem. 272*, 27517−20.
7. DeMarco, M. L., Silveira, J. R., Caughey, B., and Daggett, V. (2006) Structural Properties of Prion Protein Protofibrils and Fibrils: An Experimental Assessment of Atomic Models, *Biochemistry 45*, 15573−15582.
8. Zahn, R., Liu, A. Z., Luhrs, T., Riek, R., von Schroetter, C., Garcia, F. L., Billeter, M., Calzolai, L., Wider, G., and Wuthrich, K. (2000) NMR solution structure of the human prion protein, *Proc. Natl. Acad. Sci. U.S.A. 97*, 145−150.
9. Alonso, D. O. V., DeArmond, S. J., Cohen, F. E., and Daggett, V. (2001) Mapping the early steps in the pH-induced conformational conversion of the prion protein, *Proc. Natl. Acad. Sci. U.S.A. 98*, 2985−2989.
10. Alonso, D. O. V., An, C., and Daggett, V. (2002) Simulations of biomolecules: characterization of the early steps in the pH-induced conformational conversion of the hamster, bovine and human forms of the prion protein, *Philos. Trans. R. Soc. London, Ser. B 360*, 1165−1178.
11. DeMarco, M. L., and Daggett, V. (2004) From conversion to aggregation: Protofibril formation of the prion protein, *Proc. Natl. Acad. Sci. U.S.A. 101*, 2293−2298.
12. James, T. L., Liu, H., Ulyanov, N. B., FarrJones, S., Zhang, H., Donne, D. G., Kaneko, K., Groth, D., Mehlhorn, I., Prusiner, S. B., and Cohen, F. E. (1997) Solution structure of a 142-residue

recombinant prion protein corresponding to the infectious fragment of the scrapie isoform, *Proc. Natl. Acad. Sci. U.S.A. 94*, 10086−10091.
13. Williamson, R. A., Peretz, D., Pinilla, C., Ball, H., Bastidas, R. B., Rozenshteyn, R., Houghten, R. A., Prusiner, S. B., and Burton, D. R. (1998) Mapping the prion protein using recombinant antibodies, *J. Virol. 72*, 9413−9418.
14. Supattapone, S., Bouzamondo, E., Ball, H. L., Wille, H., Nguyen, H-B, O., Cohen, F. E., DeArmond, S. J., Prusiner, S. B., and Scott, M. (2001) A Protease-Resistant 61-Residue Prion Peptide Causes Neurodegeneration in Transgenic Mice, *Mol. Cell. Biol. 21*, 2608−2616.
15. Kitamoto, T., Iizuka, R., Tateishi, J. (1993) An amber mutation of prion protein in Gerstmann-Straussler syndrome with mutant PrP plaques, *Biochem. Biophys. Res. Commun. 192*, 525−531.
16. Guilbert, C., Ricard, F., and Smith, J. C. (2000) Dynamic simulation of the mouse prion protein, *Biopolymers 54*, 406−415.
17. Hirschberger, T., Stork, M., Schropp, B., Winklhofer, K. F., Tatzelt, J., and Tavan, P. (2006) Structural instability of the prion protein upon M205S/R mutations revealed by molecular dynamics simulations, *Biophys. J. 90*, 3908−3918.
18. Shamsir, M. S. and Dalby, A. R. (2005) One gene, two diseases and three conformations: Molecular dynamics simulations of mutants of human prion protein at room temperature and elevated temperatures, *Proteins 59*, 275−290.
19. Sekijima, M., Motono, C., Yamasaki, S., Kaneko, K., and Akiyama, Y. (2003) Molecular dynamics simulation of dimeric and monomeric forms of human prion protein: insight into dynamics and properties, *Biophys. J. 85*, 1176−85.
20. Gu, W., Wang, T., Zhu, J., Shi, Y., and Liu, H. (2003) Molecular dynamics simulation of the unfolding of the human prion protein domain under low pH and high temperature conditions, *Biophys. Chem. 104*, 79−94.
21. Gsponer, J., Ferrara, P., and Caflisch, A. (2001) Flexibility of the murine prion protein and its Asp178Asn mutant investigated by molecular dynamics simulations, *J. Mol. Graphics Modell. 20*, 169−82.
22. el-Bastawissy, E., Knaggs, M. H., and Gilbert, I. H. (2001) Molecular dynamics simulations of wild-type and point mutation human prion protein at normal and elevated temperature, *J. Mol. Graphics Modell. 20*, 145−54.
23. Langella, E., Improta, R., and Barone, V. (2004) Checking the pH-induced conformational transition of prion protein by molecular dynamics simulations: effect of protonation of histidine residues, *Biophys. J. 87*, 3623−32.
24. Parchment, O. G., and Essex, J. W. (2000) Molecular dynamics of mouse and Syrian hamster PrP: implications for activity, *Proteins 38*, 327−40.
25. Turk, E., Teplow, D. B., Hood, L. E., and Prusiner, S. B. (1988) Purification and Properties of the Cellular and Scrapie Hamster Prion Proteins, *Eur. J. Biochem. 176*, 21−30.
26. Hermann, L. M., and Caughey, B. (1998) The importance of the disulfide bond in prion protein conversion, *Neuroreport 9*, 2457−2461.
27. Yanai, A., Meiner, Z., Gahali, I., Gabizon, R., Taraboulos, A. (1999) Subcellular trafficking abnormalities of a prion protein with a disrupted disulfide loop, *FEBS Lett. 460*, 11−16.
28. Maiti, N. R., and Surewicz, W. K. (2001) The role of disulfide bridge in the folding and stability of the recombinant human prion protein, *J. Biol. Chem. 276*, 2427−2431.
29. Brown, D. R., Herms, J., and Kretzschmar, H. A. (1994) Mouse Cortical-Cells Lacking Cellular Prp Survive in Culture with a Neurotoxic Prp Fragment, *Neuroreport 5*, 2057−2060.
30. Forloni, G., Angeretti, N., Chiesa, R., Monzani, E., Salmona, M., Bugiani, O., and Tagliavini, F. (1993) Neurotoxicity of a prion protein fragment, *Nature 362*, 543−6.
31. Supattapone, S., Bosque, P., Muramoto, T., Wille, H., Aagaard, C., Peretz, D., Nguyen, H. O., Heinrich, C., Torchia, M., Safar, J., Cohen, F. E., DeArmond, S. J., Prusiner, S. B., and Scott, M. (1999) Prion protein of 106 residues creates an artifical transmission barrier for prion replication in transgenic mice, *Cell 96*, 869−78.
32. Kabsch, W., and Sander, C. (1983) Dictionary of Protein Secondary Structure—Pattern-Recognition of Hydrogen-Bonded and Geometrical Features, *Biopolymers 22*, 2577−2637.
33. Beck, D.A.C., Alonso, D.O.V., and Daggett, V. (2006). *in lucem* molecular mechanics, Computer Program, University of Washington.
34. Levitt, M., Hirshberg, M., Sharon, R., and Daggett, V. (1995) Potential-Energy Function and Parameters for Simulations of the Molecular-Dynamics of Proteins and Nucleic-Acids in Solution, *Comput. Phys. Commun. 91*, 215−231.
35. Levitt, M., Hirshberg, M., Sharon, R., Laidig, K. E., and Daggett, V. (1997) Calibration and testing of a water model for simulation of the molecular dynamics of proteins and nucleic acids in solution, *J. Phys. Chem. B 101*, 5051−5061.
36. Beck, D. A. C., and Daggett, V. (2004) Methods for molecular dynamics simulations of protein folding/unfolding in solution, *Methods 34*, 112−120.
37. Langella, E., Improta, R., Crescenzi, O., and Barone, V. (2006) Assessing the acid-base and conformational properties of histidine residues in human prion protein (125-228) by means of pK(a) calculations and molecular dynamics simulations, *Proteins 64*, 167−77.
38. Kell, G. S. (1967) Precise Representation of Volume Properties of Water at 1 Atmosphere, *J. Chem. Eng. Data 12*, 66.
39. Mills, J. E., and Dean, P. M. (1996) Three-dimensional hydrogen-bond geometry and probability information from a crystal survey, *J. Comput. Aided Mol. Des. 10*, 607−22.
40. Pettersen, E. F., Goddard, T. D., Huang, C. C., Couch, G. S., Greenblatt, D. M., Meng, E. C., and Ferrin, T. E. (2004) UCSF chimera—A visualization system for exploratory research and analysis, *J. Comput. Chem. 25*, 1605−1612.
41. Morrissey, M. P., and Shakhnovich, E. I. (1999) Evidence for the role of PrP(C) helix 1 in the hydrophilic seeding of prion aggregates, *Proc. Natl. Acad. Sci. U.S.A. 96*, 11293−8.
42. Speare, J. O., Rush, T. S., 3rd, Bloom, M. E., and Caughey, B. (2003) The role of helix 1 aspartates and salt bridges in the stability and conversion of prion protein, *J. Biol. Chem. 278*, 12522−9.
43. Ziegler, J., Viehrig, C., Geimer, S., Rosch, P., and Schwarzinger, S. (2006) Putative aggregation initiation sites in prion protein, *FEBS Lett. 580*, 2033−40.
44. Armen, R. S., DeMarco, M. L., Alonso, D. O., and Daggett, V. (2004) Does Pauling and Corey's a-pleated sheet structure may define the prefibrillar amyloidogenic intermediate in amyloid disease?, *Proc. Natl. Acad. Sci. U.S.A. 101*, 11622−11627.
45. Ziegler, J., Sticht, H., Marx, U. C., Muller, W., Rosch, P., and Schwarzinger, S. (2003) CD and NMR studies of prion protein (PrP) helix 1. Novel implications for its role in the $PrP^{C}\rightarrow PrP^{Sc}$ conversion process, *J. Biol. Chem. 278*, 50175−81.
46. Watzlawik, J., Skora, L., Frense, D., Griesinger, C., Zweckstetter, M., Schulz-Schaeffer, W. J. and Kramer, M. L. (2006) Prion protein helix1 promotes aggregation but is not converted into β-sheet, *J. Biol. Chem. 281*, 30242−30250.
47. Caughey, B. W., Dong, A., Bhat, K. S., Ernst, D., Hayes, S. F., and Caughey, W. S. (1991) Secondary Structure-Analysis of the Scrapie-Associated Protein PrP 27-30. in Water by Infrared-Spectroscopy, *Biochemistry 30*, 7672−7680.
48. Pan, K. M., Baldwin, M., Nguyen, J., Gasset, M., Serban, A., Groth, D., Mehlhorn, I., Huang, Z. W., Fletterick, R. J., Cohen, F. E., and Prusiner, S. B. (1993) Conversion of Alpha-Helices into Beta-Sheets Features in the Formation of the Scrapie Prion Proteins, *Proc. Natl. Acad. Sci. U.S.A. 90*, 10962−10966.
49. Gasset, M., Baldwin, M. A., Fletterick, R. J., and Prusiner, S. B. (1993) Perturbation of the secondary structure of the scrapie prion protein under conditions that alter infectivity, *Proc. Natl. Acad. Sci. U.S.A. 90*, 1−5.
50. Knowles, T., and Zahn, R. (2006) Enhanced stability of human prion proteins with two disulfide bridges, *Biophys. J.*
51. Mead, S. (2006) Prion disease genetics, *Eur. J. Hum. Genet. 14*, 273−281.
52. Peretz, D., Williamson, R. A., Kaneko, K., Vergara, J., Leclerc, E., Schmitt-Ulms, G., Mehlhorn, I. R., Legname, G., Wormald, M. R., Rudd, P. M., Dwek, R. A., Burton, D. R., and Prusiner, S. B. (2001) Antibodies inhibit prion propagation and clear cell cultures of prion infectivity, *Nature 412*, 739−743.
53. Matsunaga, Y., Peretz, D., Williamson, A., Burton, D., Mehlhorn, I., Groth, D., Cohen, F. E., Prusiner, S. B., and Baldwin, M. A. (2001) Cryptic epitopes in N-terminally truncated prion protein are exposed in the full-length molecule: dependence of conformation on pH, *Proteins 44*, 110−118.
54. Muramoto, T., Scott, M., Cohen, F. E. and Prusiner, S. B. (1996) Recombinant scrapie-like prion protein of 106 amino acids is soluble, *Proc. Natl. Acad. Sci. U.S.A. 93*, 15457−15462.
55. Baskakov, I. V., Aagaard, C., Mehlhom, I., Wille, H., Groth, D., Baldwin, M. A., Prusiner, S. B. and Cohen, F. E. (2000) Self-

assembly of recombinant prion protein of 106 residues, *Biochemistry 39*, 2792−2804.
56. Kaneko, K., Ball, H. L., Wille, H., Zhang, H., Groth, D., Torchia, M., Tremblay, P., Safar, J., Prusiner, S. B., DeArmond, S. J., Baldwin, M. A., and Cohen, F. E. (2000) A synthetic peptide initiates Gerstmann-Straussler-Scheinker (GSS) disease in transgenic mice, *J. Mol. Biol. 295*, 997−1007.
57. Lührs, T., Zahn, R., and Wüthrich, K. (2006) Amyloid formation by recombinant full-length prion proteins in phospholipid bicelle solutions, *J. Mol. Biol. 357*, 833−41.
58. Salmona, M., Malesani, P., DeGioia, L., Gorla, S., Bruschi, M., Molinari, A., Della Vedova, F., Pedrotti, B., Marrari, M.A., Awan, T., Bugiani, O., Forloni, G., and Tagliavini, F. (1999) *Biochem. J. 342*, 207−214.
59. Law, D. D., Bitter, H. M., Liu, K., Ball, H. L., Kaneko, K., Wille, H., Cohen, F. E., Prusiner, S. B., Pines, A., and Wemmer, D. E. (2001) *Proc. Natl. Acad. Sci. U.S.A. 98*, 11686−11690.
60. Parchi, Zou, P., W., Wang, W., Brown, P., Capellari, S., Ghetti, B., Kopp, N., Schulz-Schaeffer, W. J., Kretzschmar, H. A., Head, M. W., Ironside, J. W., Gambetti, P., and Chen, S. G. (2000) Genetic influence on the structural variations of the abnormal prion protein, *Proc. Natl. Acad. Sci. U.S.A. 97*, 10168−10172.
61. Chabry, J., Caughey, B., and Chesebro, B. (1998) Specific inhibition of in vitro formation of protease-resistant prion protein by synthetic peptides, *J. Biol. Chem. 273*, 13203−7.
62. Kundu, B., Maiti, N. R., Jones, E. M., Surewicz, K. A., Vanik, D. L., and Surewicz, W. K. (2003) Nucleation-dependent conformational conversion of the Y145Stop variant of human prion protein: Structural clues for prion propagation, *Proc. Natl. Acad. Sci. U.S.A. 100*, 12069−12074.
63. Novitskaya, V., Makarava, N., Bellon, A., Bocharova, O. V., Bronstein, I. B., Williamson, R. A., and Baskakov, I. V. (2006) Probing the conformation of the prion protein within a single amyloid fibril using a novel immunoconformational assay, *J. Biol. Chem. 281*, 15536−15545.
64. White, A. R., Enever, P., Tayebi, M., Mushens, R., Linehan, J., Brandner, S., Anstee, D., Collinge, J., and Hawke, S. (2003) Monoclonal antibodies inhibit prion replication and delay the development of prion disease, *Nature 422*, 80−3.
65. Matucci, A., Zanusso, G., Gelati, M., Farinazzo, A., Fiorini, M., Ferrari, S., Andrighetto, G., Cestari, T., Caramelli, M., Negro, A., Morbin, M., Chiesa, R., Monaco, S., and Tridente, G. (2005) Analysis of mammalian scrapie protein by novel monoclonal antibodies recognizing distinct prion protein glycoforms: an immunoblot and immunohistochemical study at the light and electron microscopic levels, *Brain Res. Bull. 65*, 155−162.
66. Eghiaian, F., Grosclaude, J., Lesceu, S., Debey, P., Doublet, B., Treguer, E., Rezaei, H., and Knossow, M. (2004) Insight into the $PrP^{C} \rightarrow PrP^{Sc}$ conversion from the structures of antibody-bound ovine prion scrapie-susceptibility variants, *Proc. Natl. Acad. Sci. U.S.A. 101*, 10254−10259.
67. Paramithiotis, E., Pinard, M., Lawton, T., LaBoissiere, S., Leathers, V. L., Zou, W. Q., Estey, L. A., Lamontagne, J., Lehto, M. T., Kondejewski, L. H., Francoeur, G. P., Papadopoulos, M., Haghighat, A., Spatz, S. J., Head, M., Will, R., Ironside, J., O'Rourke, K., Tonelli, Q., Ledebur, H. C., Chakrabartty, A., and Cashman, N. R. (2003) A prion protein epitope selective for the pathologically misfolded conformation, *Nat. Med. 9*, 893−899.

BI0619066